

Ground state properties of Na_2IrO_3 determined from *ab initio* Hamiltonian and its extensions containing Kitaev and extended Heisenberg interactions

Tsuyoshi Okubo,^{1,*} Kazuya Shinjo,^{2,3} Youhei Yamaji,⁴ Naoki
Kawashima,¹ Shigetoshi Sota,⁵ Takami Tohyama,⁶ and Masatoshi Imada⁷

¹*Institute for Solid State Physics, University of Tokyo, Kashiwa, Chiba 277-8581, Japan*

²*Yukawa Institute for Theoretical Physics, Kyoto University, Kyoto 606-8502, Japan*

³*Computational Condensed Matter Physics Laboratory, RIKEN, Saitama 351-0198, Japan*

⁴*Quantum-Phase Electronics Center (QPEC), The University of Tokyo, Tokyo, 113-8656, Japan*
⁵*Computational Materials Science Research Team,*

RIKEN Advanced Institute for Computational Science (AICS), Kobe, Hyogo 650-0047, Japan

⁶*Department of Applied Physics, Tokyo University of Science, , Tokyo 125-8585, Japan*

⁷*Department of Applied Physics, University of Tokyo, Tokyo 113-8656, Japan*

(Dated: March 6, 2024)

We investigate the ground state properties of Na_2IrO_3 based on numerical calculations of the recently proposed *ab initio* Hamiltonian represented by Kitaev and extended Heisenberg interactions. To overcome the limitation posed by small tractable system sizes in the exact diagonalization study employed in a previous study (Yamaji *et al.*, Phys. Rev. Lett. **113**, 107201 (2014)), we apply two-dimensional density matrix renormalization group, and infinite-size tensor-network method. By calculating at much larger system sizes, we critically test the validity of the exact diagonalization results. The results consistently indicate that the ground state of Na_2IrO_3 is a magnetically ordered state with zigzag configuration in agreement with experimental observations and the previous diagonalization study. Applications of the two independent methods in addition to the exact diagonalization study further uncover a consistent and rich phase diagram near the zigzag phase beyond the accessibility of the exact diagonalization. For example, in the parameter space away from the *ab initio* value of Na_2IrO_3 controlled by the trigonal distortion, we find three phases: (i) an ordered phase with the magnetic moment aligned mutually in 120 degrees orientation on every third hexagon, (ii) a magnetically ordered phase with a 16-site unit-cell, and (iii) an ordered phase with presumably incommensurate periodicity of the moment. It suggests that potentially rich magnetic structures may appear in $A_2\text{IrO}_3$ compounds for A other than Na. The present results also serve to establish the accuracy of the first-principles approach in reproducing the available experimental results thereby further contribute to find a route to realize the Kitaev spin liquid.

I. INTRODUCTION

Novel quantum phenomena induced by strong spin-orbit interaction have recently attracted much interest in condensed matter physics. Iridium oxides offer a typical example that shows rich and interesting phenomena¹⁻⁴. Among them, $A_2\text{IrO}_3$ ($A = \text{Na}$ or Li) have most intensively been investigated⁵⁻¹⁰ since the theoretical proposal that the Kitaev spin liquid would be realized^{1,2}.

The Kitaev interaction is an anisotropic Ising-like interaction, $S^\gamma S^\gamma$, with the easy axes γ depending on the direction of the interacting bonds. For the model represented only by the Kitaev interaction called Kitaev model, the ground state is proved to be a quantum spin-liquid¹¹. As a more realistic model representing Na_2IrO_3 , the so-called Kitaev-Heisenberg model with both the Heisenberg and Kitaev interactions has been proposed^{1,2}. However, it has turned out that this model does not either properly account for the experimental observation of the zigzag magnetic order stabilized at low temperatures⁶⁻⁸. In order to bridge the discrepancy between the experiments and the theoretical predictions, several alternative models have been proposed. They contain further neighbor interactions^{6,7,12-14} or ad-

ditional anisotropic interactions caused by the trigonal distortion¹⁵⁻¹⁹.

In this paper, in order to further clarify the nature of Na_2IrO_3 , we investigate the ground state of the *ab initio* Hamiltonian for Na_2IrO_3 proposed by Yamaji *et al.*¹⁸ and summarized in Appendix A. In the *ab initio* Hamiltonian, where off-diagonal anisotropic interactions due to the trigonal distortion as well as weak second-nearest neighbor and third-nearest neighbor interactions are nonzero beyond the simple Kitaev-Heisenberg Hamiltonian, the experimentally observed zigzag order was reproduced by exact diagonalizations (ED) of clusters of 24 and 32 sites^{18,20}. However, more thorough studies are desired beyond small clusters to understand intrinsic properties in the thermodynamic limit.

In the present article, we carry out larger size calculations using sophisticated numerical methods; density matrix renormalization group (DMRG) and tensor network (TN). Applicability of the newly developed TN method to *ab initio* Hamiltonians containing complex interactions beyond simple model Hamiltonians²¹, is examined by carefully comparing with the ED and DMRG. If the trigonal distortion is close to that of the *ab initio* Hamiltonian for Na_2IrO_3 , the two methods show the zigzag

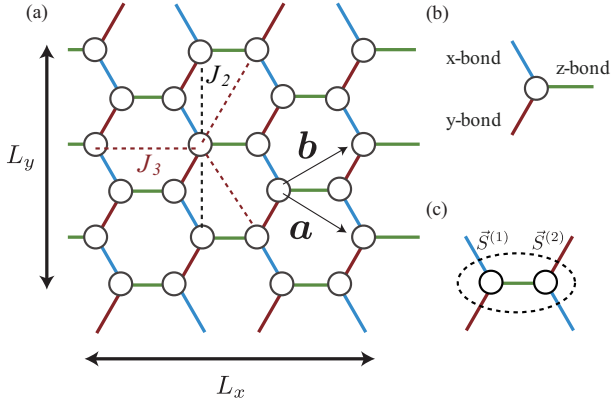


FIG. 1. (a) Two-dimensional honeycomb lattice where J_2 and J_3 represent the second- and the third-neighbor interaction pairs. In numerical calculations, we mainly use $L_x \times L_y$ lattices or unit cells with periodic boundary condition for both of L_x and L_y directions. (b) Three directions of the nearest-neighbor interactions. (c) Definition of the unit used in the classical analysis.

order consistently with the exact diagonalization results in Ref.18.

Another purpose of this study is to clarify the role of the trigonal distortion and search phases competing with the zigzag order when the trigonal distortion is deviated from that of Na_2IrO_3 . Richer phase diagram beyond the exact diagonalization is determined, where several distinct symmetry broken magnetic orders emerge, when the trigonal distortion is monitored away from Na_2IrO_3 (as introduced in Eqs. (8) and (9), later). This study may have relevance to other materials $A_2\text{IrO}_3$ for A other than Na because the trigonal distortion depends on A .

The rest of the paper is organized as follows. In Sec. II, we describe our model. In Sec. III, we present results of classical approximations. Our main results for the *ab initio* Hamiltonian and its derivatives are presented in Sec. IV. Finally, we summarize our results in Sec. V.

II. MODEL

The Hamiltonian of the model we investigate is given by

$$\mathcal{H} \equiv \mathcal{H}_{1\text{st}} + \mathcal{H}_{2\text{nd}} + \mathcal{H}_{3\text{rd}}, \quad (1)$$

where $\mathcal{H}_{1\text{st}}$, $\mathcal{H}_{2\text{nd}}$, and $\mathcal{H}_{3\text{rd}}$ express the nearest neighbor, the second neighbor, and the third neighbor interactions on the honeycomb lattice, respectively (see Fig. 1). For the nearest neighbor interaction, we consider distorted Kitaev-Heisenberg interaction with off-diagonal terms as

$$\mathcal{H}_{1\text{st}} \equiv \sum_{\Gamma=X,Y,Z} \sum_{\langle i,j \rangle \in \Gamma} \vec{S}_i^{\Gamma} J_{\Gamma} \vec{S}_j, \quad (2)$$

where Γ means the directions of the interactions and real symmetric matrices J_{Γ} ($\Gamma = X, Y, Z$) are give by

$$J_X \equiv \begin{pmatrix} K' & I_2'' & I_2' \\ I_2'' & J'' & I_1' \\ I_2' & I_1' & J' \end{pmatrix}, \quad J_Y \equiv \begin{pmatrix} J'' & I_2'' & I_1' \\ I_2'' & K' & I_2' \\ I_1' & I_2' & J' \end{pmatrix}, \quad (3)$$

$$J_Z \equiv \begin{pmatrix} J & I_1 & I_2 \\ I_1 & J & I_2 \\ I_2 & I_2 & K \end{pmatrix}.$$

For the second neighbor interactions, we consider only the interaction perpendicular to the Z bond:

$$\mathcal{H}_{2\text{nd}} \equiv \sum_{\langle\langle i,j \rangle\rangle \in Z'} \vec{S}_i^{\Gamma} J_{Z'}^{(2\text{nd})} \vec{S}_j, \quad (4)$$

where $\sum_{\langle\langle i,j \rangle\rangle \in Z'}$ represents the sum over second neighbor pairs perpendicular to the Z bond, and $J_{Z'}^{(2\text{nd})}$ is give by

$$J_{Z'}^{(2\text{nd})} \equiv J^{(2\text{nd})} = \begin{pmatrix} J^{(2\text{nd})} & I_1^{(2\text{nd})} & I_2^{(2\text{nd})} \\ I_1^{(2\text{nd})} & J^{(2\text{nd})} & I_2^{(2\text{nd})} \\ I_2^{(2\text{nd})} & I_2^{(2\text{nd})} & K^{(2\text{nd})} \end{pmatrix}. \quad (5)$$

Finally, for the third neighbor interaction the Hamiltonian is given by

$$\mathcal{H}_{3\text{rd}} \equiv \sum_{\Gamma=X,Y,Z} \sum_{\langle\langle\langle i,j \rangle\rangle\rangle \in \Gamma} \vec{S}_i^{\Gamma} J_{\Gamma} \vec{S}_j, \quad (6)$$

where $\sum_{\langle\langle\langle i,j \rangle\rangle\rangle \in \Gamma}$ represents the sum over the third neighbor pairs parallel to the Γ direction ($\Gamma = X, Y, Z$). We consider only the isotropic Heisenberg interaction for the third neighbor interaction:

$$J_{\Gamma}^{(3\text{rd})} \equiv J^{(3\text{rd})} = \begin{pmatrix} J^{(3\text{rd})} & 0 & 0 \\ 0 & J^{(3\text{rd})} & 0 \\ 0 & 0 & J^{(3\text{rd})} \end{pmatrix}. \quad (7)$$

The above spin Hamiltonian has been derived from the *ab initio* Hamiltonian for t_{2g} electrons of iridium atoms in Na_2IrO_3 :

$$\hat{H}_{t_{2g}} = \hat{H}_0 + \hat{H}_{\text{tri}} + \hat{H}_{\text{SOC}} + \hat{H}_U, \quad (8)$$

where \hat{H}_0 , \hat{H}_{tri} , \hat{H}_{SOC} and \hat{H}_U represent the hopping term, the trigonal distortion with orbital-dependent chemical potentials, the spin-orbit coupling and the Coulomb term, respectively¹⁸. Due to the trigonal distortion term, the spin Hamiltonian does not possess the symmetry among spin components S_x, S_y, S_z ; only S_x and S_y remain symmetric. Thus, the global symmetries of the Hamiltonian are the Z_2 time-reversal symmetry, the Z_2 symmetry against exchange of S_x and S_y , and the lattice translational symmetry. By using a vector representation of the electron creation operators at site

i , $\vec{c}_i^\dagger = (\hat{c}_{i,yz,\uparrow}^\dagger, \hat{c}_{i,yz,\downarrow}^\dagger, \hat{c}_{i,zx,\uparrow}^\dagger, \hat{c}_{i,zx,\downarrow}^\dagger, \hat{c}_{i,xy,\uparrow}^\dagger, \hat{c}_{i,xy,\downarrow}^\dagger)$, the trigonal distortion term is expressed as

$$\hat{H}_{\text{tri}} = \sum_i \vec{c}_i^\dagger \begin{bmatrix} -\mu_{yz} & \Delta & \Delta \\ \Delta & -\mu_{zx} & \Delta \\ \Delta & \Delta & -\mu_{xy} \end{bmatrix} \hat{\sigma}_0 \vec{c}_i, \quad (9)$$

where $\hat{\sigma}_0$ is the 2×2 identity matrix. The *ab initio* values of $\mu_{yz}, \mu_{zx}, \mu_{xy}$ and Δ for Na_2IrO_3 were estimated as $\mu_{xy} - \mu_{zx} = 35$ meV, $\mu_{yz} \simeq \mu_{zx}$ and $\Delta = -28$ meV¹⁸.

All interactions for Na_2IrO_3 have been determined based on the second-order perturbation theory by using the strong-coupling expansion applied to the first principles Hamiltonian¹⁸ (see Appendix A). Based on the exact diagonalization for small clusters, Yamaji *et al* have shown that the ground state of the Hamiltonian for Na_2IrO_3 is expected to be a magnetically ordered state with the zigzag configuration consistently with the experimental observations. Within the diagonalization of small clusters, they have also determined the phase diagram in the parameter space of the trigonal distortion monitored around the *ab initio* value of Na_2IrO_3 , and have shown that several distinct magnetically ordered states emerge depending on the amplitude of the trigonal distortion¹⁸. However, the system size in the previous exact diagonalization is only up to 24 sites, and is too small for establishing properties in the thermodynamic limit. Thus, in order to verify the conclusion of the previous work and further clarify the nature of the *ab initio* Hamiltonian that contains anisotropic Kitaev-Heisenberg interaction, we clearly need to investigate larger system sizes. In the following sections, we clarify the ground state properties in the thermodynamic limit derived from results of much larger system sizes including the infinite-size calculations. We focus on the two problems; properties of the *ab initio* Hamiltonian for Na_2IrO_3 in comparison with the experimental results and the phase diagram of the Hamiltonian obtained by monitoring the trigonal distortion Δ away from the *ab initio* value, because Δ is an experimentally tunable control parameter by pressure or elemental substitutions.

III. CLASSICAL APPROXIMATION

We first consider the classical ground state, motivated by the fact that the system has a magnetic order in the experimentally observed ground state. In particular, the classical analysis provides us with insight complementary to the quantum analysis, because it enables studies on incommensurate order, whereas it is hard to capture within the framework of the TN or DMRG in which commensurability is assumed.

In the case of the classical Heisenberg spins, where \vec{S}_i is a unit vector with three components, the candidates of the ground state is obtained from the Fourier transform of exchange interactions. Suppose two spins connected by the z -bond on the honeycomb lattice as a unit (see

Fig. 1(c)). Because the Hamiltonian retains the translational symmetry based on such units constituting the triangular lattice, the Hamiltonian is diagonalized by the Fourier transform as

$$\mathcal{H}_{\text{cl}} = \frac{1}{2} \sum_{\mathbf{q}} \vec{S}_{-\mathbf{q}}^T \mathcal{J}_{\mathbf{q}} \vec{S}_{\mathbf{q}}, \quad (10)$$

where $\sum_{\mathbf{q}}$ is the summation over the wavevectors in the Brillouin zone. $\mathcal{J}_{\mathbf{q}}$ is the 6×6 Hermitian matrix representing the Fourier transform of the exchange interaction and it is given by

$$\begin{aligned} \mathcal{J}_{\mathbf{q}} &\equiv \begin{pmatrix} A & B \\ B^\dagger & A \end{pmatrix} \\ A &= 2J^{(2\text{nd})} \cos \mathbf{q} \cdot (\mathbf{a} - \mathbf{b}) \\ B &= J_x e^{-i\mathbf{q} \cdot \mathbf{a}} + J_y e^{-i\mathbf{q} \cdot \mathbf{b}} + J_z \\ &\quad + J^{(3\text{rd})} \left[2 \cos \mathbf{q} \cdot (\mathbf{a} - \mathbf{b}) + e^{-i\mathbf{q} \cdot (\mathbf{a} + \mathbf{b})} \right], \end{aligned} \quad (11)$$

where $\vec{S}_{\mathbf{q}}$ is the Fourier transform of spins in a unit

$$\vec{S}_{\mathbf{q}} \equiv \begin{pmatrix} \vec{S}_i^{(1)} \\ \vec{S}_i^{(2)} \end{pmatrix}. \quad (12)$$

By diagonalizing the exchange matrix $\mathcal{J}_{\mathbf{q}}$ numerically, we obtain candidates of the classical ground states as the lowest eigen mode. However, note that the obtained eigenvector is not necessarily the ground state because it may not satisfy the fixed length condition of classical spins; $|\vec{S}_i^{(1)}| = 1$ and $|\vec{S}_i^{(2)}| = 1$ for each site on the lattice. Instead, the lowest eigen mode can be regarded as the ground state in the spherical approximation $\sum_i |\vec{S}_i|^2 = 2N$. When the wavevector of the lowest eigen mode is incommensurate to the lattice, the eigen vector generally does not satisfy the fixed length condition. In such cases, a commensurate order, which usually satisfies the fixed length condition, close to the incommensurate wavevector often appears as the true ground state by recovering the fixed length condition.

In Fig. 2(a), we plotted the wavevector of the lowest energy mode as a function of the trigonal distortion Δ . We see that in the most part of the parameter Δ , the lowest eigen mode appears at wavevectors incommensurate to the lattice (see Fig. 2(b)). However, for -20 meV $\lesssim \Delta \lesssim -10$ meV we find that the commensurate zigzag(Z) order is the ground state, where the ferromagnetically-ordered chains consist of X and Y -bonds while these chains are anti-ferromagnetically coupled by the Z -bonds (see Fig. 3(a)). Note that the *ab initio* value for the distortion of Na_2IrO_3 is $\Delta \simeq -28$ meV, which is in the vicinity of the zigzag(Z) phase boundary.

The obtained Δ dependence of the wave vector clearly indicates that the incommensurate region consists of three distinct phases (see Fig. 2 (a)). For large negative Δ , the lowest energy states are characterized by the

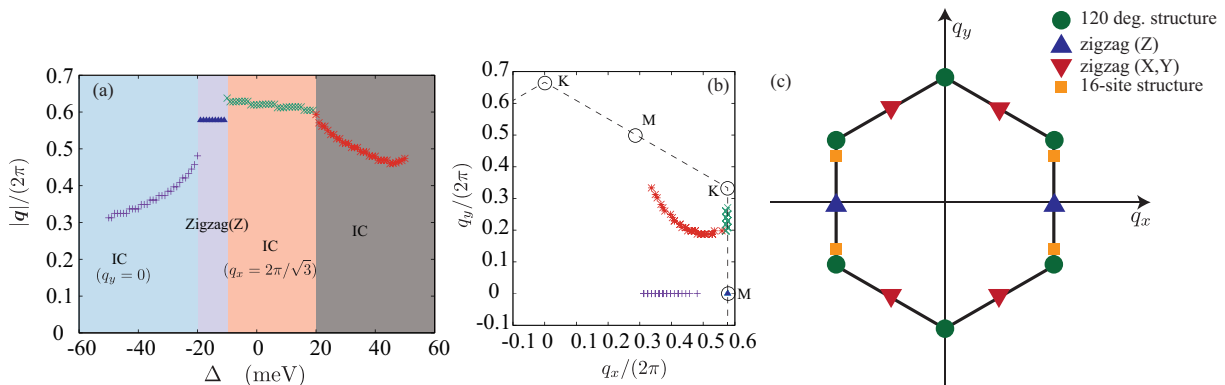


FIG. 2. (a) Classical phase diagram within the spherical approximation in the parameter space of the trigonal distortion around the *ab initio* value. The symbols represent the amplitude of the wavevectors for the ground state. (b) The position of the ground-state wavevectors. The symbols (colors) follows the notation in (a). The dashed lines represent the boundaries of the first Brillouin zone and the circles indicate high symmetric points. (c) The Bragg peak positions of several magnetic orders that appear in the present *ab initio* Hamiltonian (see also Fig. 3)

wavevectors $q_y = 0$ (the IC($q_y = 0$) phase), which move toward the M point characterizing the zigzag(Z) state. Around $\Delta = 0$, the Bragg wave number of the lowest energy states is located on the line connecting the M and K points (the IC($q_x = 2\pi/\sqrt{3}$) phase). Note that the M point represents the zigzag phase while the K point is the Bragg point for the 120 degree phase. Finally, for large Δ the lowest energy state appears inside the first Brillouin zone (the IC phase). Note that at the phase boundary between the zigzag(Z) and the IC ($q_x = 2\pi/\sqrt{3}$) phases, the characteristic wavevector discontinuously changes from the M point to a vicinity of the K point. Thus, at the boundary the phase transition is expected to be of the first order. On the other hand, the wavevector changes continuously without a jump between IC($q_y = 0$) and the zigzag(Z), and also between the IC($q_x = 2\pi/\sqrt{3}$) phase and the IC phase. Although the wavevector looks varying steeply in the former case, it is likely to be continuous because the wavevector looks naturally connected to the M point. For these boundaries, the phase transitions could be continuous.

Although the classical ground state within the spherical approximation is characterized by the incommensurate wavenumber (IC ($q_x = 2\pi/\sqrt{3}$) phase), it is close to the commensurate 120 degree structure near the phase boundary to the zigzag phase. In fact, it was claimed to be the ground state in a simple classical model proposed by Rau *et al.*,^{16,19}: They considered the classical Kitaev-Heisenberg model with an additional I_1 term, *e.g.* $S_x S_y$ interaction on z -bonds. In their model, the 120 degree structure appears as the ground state for a region with the antiferromagnetic Kitaev coupling and the antiferromagnetic Heisenberg coupling with finite I_1 term. Although they have not discussed details of this 120 degree structure, in their model, it is actually degenerate with states that have any relative angles between the clusters consisting of three neighboring sites of a site, where the three sites are aligned mutually with 120 degrees (see ex-

amples in Figs. 3(c) and (d)). When we set zero relative angle, we obtain a state that has a unit-cell containing 3 sites, which we call 3-site structure (Fig. 3(c)). (A similar terminology will be used below for larger unit-cell structures.). On the other hand, the relative angle of 180 degrees makes a 6-site structure (Fig. 3(d)). Furthermore any value of the relative angle produces a ground state. Note that the classical ground state within the spherical approximation does not contain the 120-degree commensurate phase, but the IC ($q_x = 2\pi/\sqrt{3}$) order replaces it, although they are close in energy. Such degeneracy among various 120-degree orders is often lifted by thermal or quantum fluctuations by the so called order-by-disorder mechanism²². Actually, our classical Monte Carlo calculation of the Rau's model shows that either the 3-site or the 6-site 120-degree commensurate order is selected at finite temperatures depending on the sign of K and I_1 . Thus, we expect that if the commensurate 120-degree order is stabilized instead of the IC ($q_x = 2\pi/\sqrt{3}$) order in the present *ab initio* Kitaev-Heisenberg Hamiltonian with $S = 1/2$ quantum spins, it could be either the 3-site or the 6-site structures, as reported in previous 24-site exact-diagonalization calculations¹⁸.

In addition, we also expect that other types of magnetic order may be stabilized because incommensurate wavevectors plotted in Fig. 2 are close to some commensurate values. For example, in the IC($q_x = 2\pi/\sqrt{3}$) region, the wavevectors are located in the vicinity of $\vec{q}/2\pi = (1/\sqrt{3}, 1/4)$ and $\vec{q}/2\pi = (1/\sqrt{3}, 1/5)$ which corresponds to a 16-site structure and a 20-site structure, respectively. Unfortunately, these large unit-cell structures are not fitted to 24-site cluster used in previous ED calculation¹⁸. In order to investigate stability of such structures, we need larger unit-cells beyond ED.

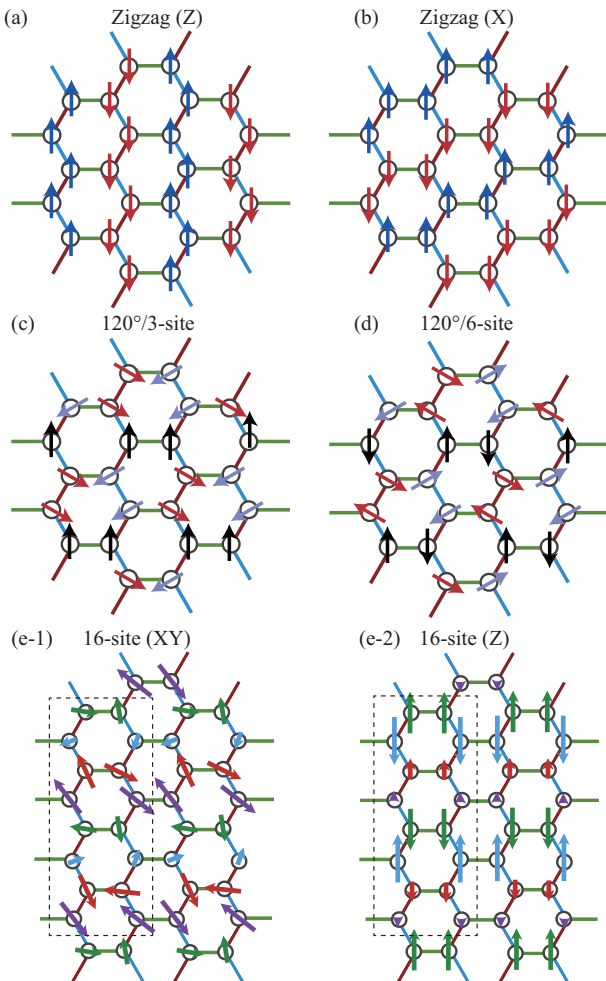


FIG. 3. Schematic views of magnetically ordered states emerging in the present *ab initio* quantum Hamiltonian and its extensions containing Kitaev and extended Heisenberg interactions: (a) zigzag(Z), (b) zigzag(X), (c) 120 degree structure with 3-site structure, (d) 120 degree structure with 6-site structure, and (e-1) *xy* components and (e-2) *z* components of the 16-site structure. For the 16-site structure, dashed rectangles indicate a magnetic unit cell.

IV. GROUND STATE PROPERTIES

A. Methods

In order to investigate the ground state property of the Hamiltonian in the presence of strong quantum fluctuations, we conduct three types of numerical calculations based on the ED, two-dimensional DMRG and tensor network based methods.

Our ED calculations were done up to 32-site based on the Lanczos algorithm. A part of the results has already been reported in Ref. 18. In order to investigate larger systems, we use a two-dimensional DMRG method where we represent the ground state wave function as a matrix product states (MPS) and variationally optimize the

wave-function parameters so as to minimize the energy²³. In the DMRG calculation, we investigate $L_x \times L_y$ lattice systems with periodic boundary conditions along both of L_x and L_y directions (see Fig. 1(a)). We keep 1000 states in DMRG processes and perform more than 10 sweeps, resulting in a typical truncation error 10^{-5} or smaller.

The ED and DMRG are quite accurate for finite systems. The maximum size they can treat is, however, restricted to about 100 sites, which are a little too small to clarify the thermodynamic properties beyond reasonable doubt. In order to investigate the property in the thermodynamic limit further, we also conduct recently developed tensor network methods which can treat infinite-size system directly. Here we use the tensor network ansatz for infinite-size systems so called infinite Projected Entangled Pair State (iPEPS)^{24–26} or infinite Tensor Product State (iTPS)^{27,28} as the ansatz of the ground state wave function. We assume infinitely repeated $L_x \times L_y$ unit-cell structure, *i.e.* $L_x \times L_y$ independent tensors with bond-dimensions D , which is the same shape with the lattice shape used in DMRG (Fig. 1). Note that the unit-cell structure used in iPEPS allows the ground state that spontaneously breaks the lattice translational symmetry in the thermodynamic limit with the periodicity taken into account up to the unit cell size. Thus, even if we assume a finite $L_x \times L_y$ unit-cell structure, a wave function represented by iPEPS is that of the infinite system without any finite size boundary effects. For the optimization of the tensors, we use the imaginary-time evolution with so called the simple update technique²⁹, which is extended to treat the second- and third-neighbor interactions (see Appendix B). Reliability of the simple update optimization is demonstrated by comparing with the full update^{26,30} for the nearest-neighbor *ab initio* Hamiltonian in Appendix C. After obtaining optimized tensors, we calculated physical quantities by using the corner transfer matrix method^{30–36}. In the following calculations, we use the bond dimension $D \leq 9$ for the case of the *ab initio* value of Na_2IrO_3 and $D \leq 6$ for the case of the trigonal distortion controlled away from the *ab initio* value.

B. Ground state of Na_2IrO_3

First, we examine the ground state of the Hamiltonian at the *ab initio* matrix elements in Eq. (8) for Na_2IrO_3 obtained by a first principles calculation¹⁸. Based on the second order perturbation theory, we can evaluate the exchange interactions as a function of Δ ¹⁸. For Na_2IrO_3 , the *ab initio* value of the trigonal distortion was calculated as $\Delta = -28$ meV, and estimated interactions of the Hamiltonian are listed in Table I (see also Appendix A). At this value, 24-site ED calculation predicts that the ground state is the zigzag(Z) state where the ferromagnetically-ordered chains consist of *X* and *Y*-bonds while these chains are antiferromagnetically coupled by the *Z*-bonds (see Fig. 3(a))¹⁸.

$J_{X,Y}$ (meV)	K'	J'	J''	I'_1	I'_2	I''_2
	-23.9	2.0	3.2	1.8	-8.4	-3.1
J_Z (meV)	K	J	I_1	I_2		
	-30.7	4.4	-0.4	1.1		
J_2 (meV)	$K^{(2nd)}$	$J^{(2nd)}$	$I_1^{(2nd)}$	$I_2^{(2nd)}$		
	-1.2	-0.8	1.0	-1.4		
J_3 (meV)	$J^{(3rd)}$					
	1.7					

TABLE I. Kitaev and extended Heisenberg exchange interactions derived from the second-order perturbation theory applied to the *ab initio* Hamiltonian at $\Delta = -28$ meV¹⁸

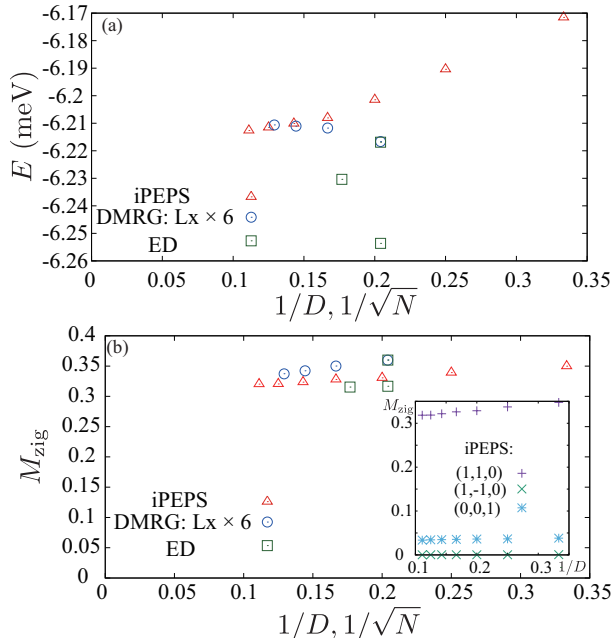


FIG. 4. Bond-dimension (D) or system size (N) dependences of the ground-state energy (a), and zigzag(Z) order parameter (b) calculated by ED, DMRG and iPEPS for the *ab initio* Hamiltonian of Na_2IrO_3 , where the Kitaev and extended Heisenberg interactions are derived from the *ab initio* value $\Delta = -28$ meV. The inset of (b) shows the amplitude of $\langle \vec{M}_{\text{zig}(Z)} \rangle$ projected onto $(x, y, z) = (1, 1, 0)$, $(1, -1, 0)$ and $(0, 0, 1)$ directions obtained by iPEPS ($D = 9$).

In Fig. 4(a), we show the energies calculated by ED, DMRG, and iPEPS as a function of the $1/\sqrt{N}$ (ED, DMRG) or $1/D$ (iPEPS). In the case of iPEPS, we used $L_x \times L_y = 4 \times 6$ unit cell. We see that the energies calculated by different methods are consistent with each other and they seem to reach a common value, $E \simeq -6.22$ meV in the limit of $D, N \rightarrow \infty$.

In order to further clarify the nature of the ground state, we plot in Fig 4(b) the order parameter of the zigzag(Z) state defined as

$$\vec{M}_{\text{zig}(Z)} \equiv \frac{1}{2}(\vec{\sigma}_1 - \vec{\sigma}_2), \quad (13)$$

where σ_α ($\alpha = 1, 2$) represents the average of spins over the equivalent sites in zigzag(Z) state (see Fig. 3(a)). In the cases of ED and DMRG we plot $M_{\text{zig}(Z)} = \sqrt{\langle \vec{M}_{\text{zig}(Z)}^2 \rangle}$, while in the case of iPEPS we plotted $M_{\text{zig}(Z)} = \sqrt{\langle \vec{M}_{\text{zig}(Z)} \rangle^2}$. Note that these two definitions should reach the same thermodynamic limit. One can clearly see that $M_{\text{zig}(Z)}$ takes a large finite value and remains nonzero in the limit of $D, N \rightarrow \infty$, indicating that zigzag(Z) state is stabilized as the ground state in the thermodynamic limit. Thus, the previous proposition that the ground state of the *ab initio* Hamiltonian of Na_2IrO_3 is the zigzag(Z) state has been established beyond reasonable doubt. In the inset of Fig. 4(b), we also plot the amplitude of $\langle \vec{M}_{\text{zig}(Z)} \rangle$ projected onto $(x, y, z) = (1, 1, 0)$, $(1, -1, 0)$ and $(0, 0, 1)$ directions obtained by iPEPS. We see that the $(1, 1, 0)$ component is dominant rather than $(1, -1, 0)$ and $(0, 0, 1)$ components. Similar results have been reported based on the pinning field analysis of ED in the previous study¹⁸. Thus the ordered moment in this zigzag(Z) state is nearly along $(1, 1, 0)$ direction in the effective spin basis, although it has also weak ($< 15\%$) $(0, 0, 1)$ component.

From x-ray resonant-magnetic-scattering experiments, the ordered moment in the low temperature phase of Na_2IrO_3 was estimated to be located in the ac plane^{5,8}. Because $(1, 1, 0)$ direction in the effective spin model is converted to $(1, 1, 0)$ direction in the real space¹⁸, which is on the ac plane of Na_2IrO_3 , the predicted ordered spin direction is consistent with the experimental observation. On the other hand, further quantitative analysis of the experimental data suggested that the ordered moment was almost parallel to the a axis^{5,8}, which was $(1, 1, -2)$ directions in the real space. Thus, ordered spin direction $(1, 1, 0)$ predicted from the *ab initio* Hamiltonian does not completely match the experimental observation. In order to reproduce the ordered-moment direction more precisely, we might need to take into account the coupling between the honeycomb layers, which is ignored in the present *ab initio* Hamiltonian¹⁸.

C. Phase diagram for parameters away from the *ab initio* trigonal distortion

Next, we discuss the ground-state phase diagram in the parameter space of the trigonal distortion monitored around the *ab initio* value $\Delta = -28$ meV. Once we set Δ , one can calculate the exchange couplings as a function of Δ through the second-order perturbation theory¹⁸. As expected from the classical analysis, we need to keep in mind that magnetically ordered ground states stabilized by controlling the trigonal distortion are subject to have large unit cells including periodicity that is incommensurate to the lattice. In order to obtain the true ground state, we examine the dependence on the system size (DMRG) and on the assumed unit cell size and structure (iPEPS). We then take the lowest energy state among

various choices as the ground state.

In Fig. 5, we show the phase diagram that is determined from consistent results of DMRG and iPEPS calculations, together with the energies and their derivatives calculated by iPEPS and DMRG. In the phase diagram, we find four types of magnetically ordered states.

For $\Delta \lesssim -3$ meV, the zigzag state is stabilized. The zigzag phase is separated in two types depending on the direction of ferromagnetically-ordered chains. For $\Delta \lesssim -44$ meV the ferromagnetically-ordered chains are perpendicular to the X -bond or to the Y -bond (zigzag(X) and zigzag(Y) states, respectively), while for -44 meV $\lesssim \Delta \lesssim -3$ meV they are perpendicular to the Z -bond (See Figs. 3 (a),(b)). This zigzag(Z) phase contains the *ab initio* value of Na_2IrO_3 , $\Delta = -28$ meV. When we increase Δ , the 120 degree structure is stabilized for -3 meV $\lesssim \Delta \lesssim -1$ meV. Whereas the previous 24-site ED calculation suggested that the 120 degree structure survives for larger trigonal distortion $\Delta < 40$ meV¹⁸, the new results based on iPEPS and DMRG reliably show that the 16-site structure characterized by the wavevector $\mathbf{q}/2\pi = (1/\sqrt{3}, 1/4)$ (see Fig. 2(c)) is stabilized for -1 meV $\lesssim \Delta \lesssim 30$ meV. Finally, for even larger Δ values ($\Delta \gtrsim 30$ meV), large unit-cell magnetic structures appear as the ground state. As is indicated by the anomaly around 45 meV in the iPEPS result of $dE/d\Delta$, there are at least two types of states in this region. These two states have the 48-site magnetic unit-cells with different shapes, which are equal to unit-cell size used in the iPEPS calculation (6×8) or a half of the size (8×12). Comparing the two states with the classical states in Fig. 2 (a), we speculate that the ground state in this region is incommensurate to the periodicity of the honeycomb lattice in the thermodynamic limit. The reason why only the two states are observed may be attributed to the limited sizes allowed for the iPEPS unit cell.

In order to see these magnetic orders clearly, we define the order parameter through the spin structure factor as

$$M(\mathbf{q}) \equiv \sqrt{\frac{1}{N} \sum_{\gamma=x,y,z} \sum_{i=1}^N \langle \hat{S}_0^\gamma \hat{S}_i^\gamma \rangle \cos(\mathbf{q} \cdot \mathbf{r}_i)}. \quad (14)$$

In the case of iPEPS, we use

$$M(\mathbf{q}) \equiv \sqrt{\sum_{\gamma=x,y,z} \left| \frac{1}{N} \sum_{i=1}^N \langle \hat{S}_i^\gamma \rangle e^{i\mathbf{q} \cdot \mathbf{r}_i} \right|^2}. \quad (15)$$

Because the wave function obtained by iPEPS is that of the infinite system, we calculate $M(\mathbf{q})$ of iPEPS approximately by using the 96×96 finite lattice. In Fig. 6, we plot $M(\mathbf{q})$ s corresponding to zigzag(Z), zigzag(X) (and zigzag(Y)), 120 degree structure and 16-site order together with the 48-site order representing the incommensurate region in the phase diagram. The Bragg wavevec-

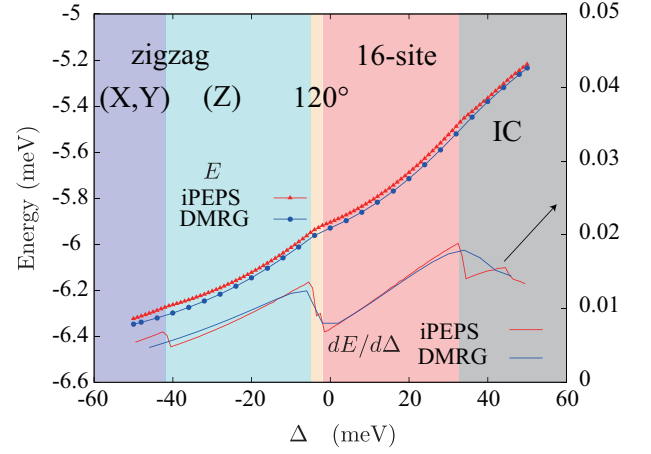


FIG. 5. Phase diagram in parameter space of trigonal distortion around *ab initio* Hamiltonian represented by Kitaev and extended Heisenberg interactions for Na_2IrO_3 . Red triangles and blue circles represent the energies calculated by iPEPS with $D = 6$ and DMRG for the 6×8 lattice, respectively. In the case of iPEPS we calculated the energy for 4×4 , 6×8 , 6×10 , and 8×12 unit cells and took the lowest energy state among them as the ground state. The derivatives of the energies with respect to Δ are also shown by solid curves without symbols to gain insight into the positions of the phase transitions.

tors for each state is given as

$$\frac{\mathbf{q}}{2\pi} = \begin{cases} \left(\frac{1}{2\sqrt{3}}, \frac{1}{2} \right), \left(-\frac{1}{2\sqrt{3}}, \frac{1}{2} \right) & (\text{zigzag}(X, Y)) \\ \left(\frac{1}{\sqrt{3}}, 0 \right) & (\text{zigzag}(Z)) \\ \left(\frac{1}{\sqrt{3}}, \frac{1}{3} \right) & (120 \text{ deg.}) \\ \left(\frac{1}{\sqrt{3}}, \frac{1}{4} \right) & (16\text{-site}) \\ \left(\frac{3}{4\sqrt{3}}, \frac{1}{3} \right) & (48\text{-site}) \end{cases} . \quad (16)$$

One can see that corresponding order parameters become finite in each phase, which ensures the stability of the identified phases. Note that the order parameters at the phase boundaries remain at large nonzero values before the transition to zero indicating the first order nature of the phase transitions. In case of the DMRG, the finite-size effects smears the jump to some extent.

In the following, we investigate details of each phase in the phase diagram.

1. zigzag phase

As we have shown in the phase diagram, two types of zigzag states are stabilized in the negatively large Δ region. In the vicinity of the phase boundary, we can obtain both of the zigzag(X, Y) and the zigzag(Z) states depending on the unit-cell structures and/or the initial conditions of the tensors in the iPEPS, at least as a metastable states. Thus, we can locate the first-order

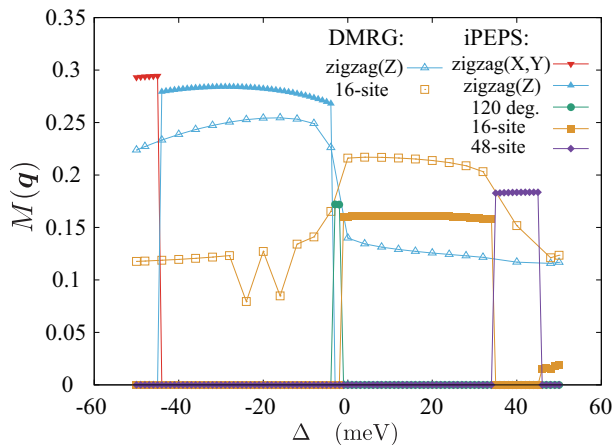


FIG. 6. Order parameters $M(\mathbf{q})$ as a function of trigonal distortion. For the nature of the wavevector characterizing each state, see the main text (See also Fig. 2(c) for the Bragg wave number of each order). In the case of DMRG, we use 6×8 lattice. Thus, we only plot the order parameter commensurate to 6×8 lattice in the case of DMRG.

phase boundary at the point where the two energy curves cross each other. In Fig. 7 (a), we plot the energies of the zigzag(X,Y) state and zigzag(Z) state obtained by the iPEPS. We see a clear energy crossing around $\Delta = -44$ meV indicating the first-order phase transition between the zigzag(X,Y) phase and the zigzag(Z) phase.

In the DMRG for 6×8 cluster, there is no clear anomaly around $\Delta = -44$ meV in the energy and the order parameters (see Figs. 5 and 6). Because 6 cluster does not fit the zigzag(X,Y) structure, the zigzag(Z) state is probably stabilized in wider region than the iPEPS.

Note that the degeneracy of the ground states is different between the zigzag(X,Y) and the zigzag(Z) phases; four-fold degeneracy for the zigzag(X,Y) state, while two-fold for the zigzag(Z) state. Thus we expect finite-temperature phase transitions with the Z_4 symmetry breaking for the zigzag(X,Y) phase, distinct from the Z_2 symmetry breaking for the zigzag(Z) state.

2. 120 degree phase

Next we focus on the phase with the 120 degree structure. In Fig. 7(b), we plot the energies of the zigzag(Z), the 120 degree, and the 16-site states as a function of Δ . For -3 meV $\lesssim \Delta \lesssim -1$ meV, the 120 degree state has the lowest energy. Although, the range of the 120 degree structure is largely reduced from the previous estimate based on the 24-site ED calculation¹⁸, the data show that the 120 degree structure phase survives.

Although the 120 degree structure does not fit 6×8 cluster used in DMRG, we observed that in DMRG for 8×6 cluster the 120 degree structure appears and around $\Delta = 0$ meV its energy is lower than that of 6×8 cluster. This observation also indicates that around $\Delta = 0$ meV,

the 120 degree structure is stabilized rather than the 16-site structure.

As we mentioned in Sec. III, in the case of the simple Rau's model, the classical 120 degree state is highly degenerated including 3-site and 6-site states in Fig. 3 (c,d). In the case of the present *ab initio* Hamiltonian, the 120 degree state is expected to be slightly distorted from 120 degrees structure by varying the canting angle because of the anisotropy. Then the quantum fluctuation and the distortion would lift the degeneracy between 3-site and 6-site states, and one of them could be realized as the ground state. Although it is difficult to determine which structure is actually realized in the ground state from finite-size calculations that prohibit spontaneous symmetry breaking, we can investigate the structures of infinite system using iPEPS where we observe the spontaneous symmetry breaking measured by a nonzero local magnetization.

In order to investigate the magnetic structure, we study the relative angle ϕ between two spins connected by z -bond, which is defined as

$$\cos(\phi) \equiv \frac{\langle \vec{S}^{(1)} \rangle \cdot \langle \vec{S}^{(2)} \rangle}{|\langle \vec{S}^{(1)} \rangle| |\langle \vec{S}^{(2)} \rangle|}. \quad (17)$$

In the ideal 120 degree structure, $\cos(\phi)$ takes three values depending on the position. For the 3-site and the 6-site structures, they are

$$\cos(\phi) = \begin{cases} (1, -1/2, -1/2) & \text{3-site} \\ (-1, 1/2, 1/2) & \text{6-site.} \end{cases} \quad (18)$$

In the iPEPS, we obtained two sets of $\cos(\phi)$ depending on the initial conditions: They are $\cos \phi = (-0.98, 0.75, 0.58)$ and $\cos \phi = (1.00, -0.25, -0.26)$ at $\Delta = -2$ meV. Based on the comparison with the expected values of the 3-site and the 6-site structures, we interpret that the states obtained by iPEPS correspond to 3-site and 6-site states with distortion caused by the anisotropy. The energy of the expected 6-site state is slightly lower than that of the 3-site state. However, the energy difference is only $\Delta \simeq 0.0003$ meV which seems to be smaller than the numerical errors that arise from the imaginary-time evolution with finite time steps²⁹ and the approximate contraction of the infinite tensor network^{30,35,36}. Thus, based on the present numerical data, we only conclude that the 3-site state or the 6-site state are realized as the ground states in the 120 degree phase.

Both of the 3-site and 6-site 120 degree states are six-fold degenerate: Z_3 from the lattice translation and Z_2 from the time reversal symmetries. Thus, one can expect a finite-temperature phase transition with breaking of the Z_6 symmetry, which is usually a successive Berezinskii-Kosterlitz-Thouless (BKT) transitions. By decreasing the temperature from the high temperature paramagnetic phase, a BKT transition occurs at $T = T_{c1}$ and quasi long-range ordered phase of an emergent $U(1)$

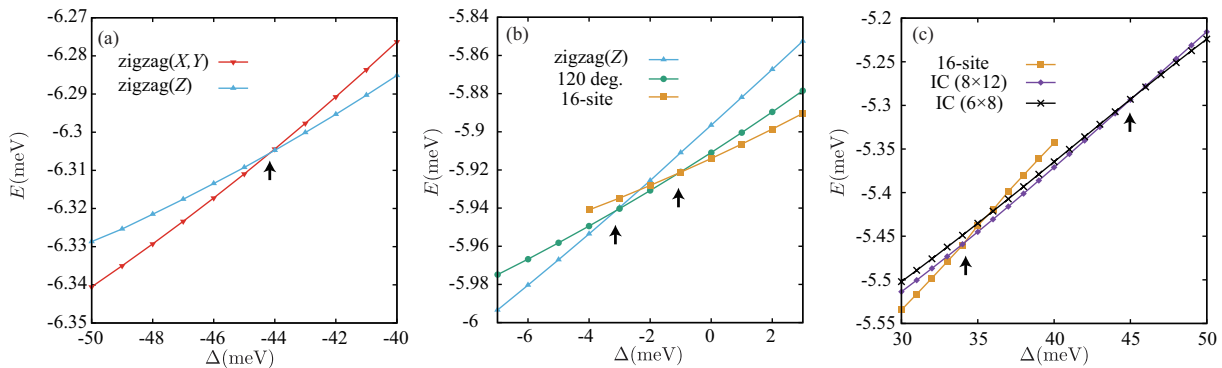


FIG. 7. (Color online) Energies obtained by iPEPS in the vicinity of phase boundaries. (a) Phase boundary between the zigzag(X, Y) and zigzag(Z) phases. (b) Phase boundaries of the 120 degree phase. (c) Phase boundaries of the IC phase. The arrows indicate the positions of the phase boundaries.

symmetry appears in $T_{c2} < T < T_{c1}$. Below the second BKT transition temperature T_{c2} , the magnetic long-range order with breaking Z_6 symmetry is expected to be stabilized³⁷.

3. 16-site phase

Based on the DMRG and iPEPS, we found that the 16-site state, which has not been reported in the previous analyses, is stabilized in a wide region of the phase diagram. Here we investigate the magnetic structure of the 16-site state.

As we mentioned, the 16-site state is characterized by the wavevector $\mathbf{q}^*/2\pi = (1/\sqrt{3}, 1/4)$. Using the wavevector \mathbf{q}^* , the local magnetizations obtained from iPEPS are well reproduced by

$$\langle \vec{S}^{(1)}(\mathbf{r}) \rangle = \begin{pmatrix} r_{xy} \cos(\mathbf{q} \cdot \mathbf{r} + \theta + \alpha) \\ r_{xy} \cos(\mathbf{q} \cdot \mathbf{r} - \theta + \alpha) \\ r_z \cos(\mathbf{q} \cdot \mathbf{r} + \alpha) \end{pmatrix} \quad (19)$$

and

$$\langle \vec{S}^{(2)}(\mathbf{r}) \rangle = \begin{pmatrix} r_{xy} \cos(\mathbf{q} \cdot \mathbf{r} - \theta + \alpha) \\ r_{xy} \cos(\mathbf{q} \cdot \mathbf{r} + \theta + \alpha) \\ r_z \cos(\mathbf{q} \cdot \mathbf{r} + \alpha) \end{pmatrix}, \quad (20)$$

where $\vec{S}^{(1)}(\mathbf{r})$ and $\vec{S}^{(2)}(\mathbf{r})$ are two spins in the unit defined in Fig. 1(c) located at \mathbf{r} . Note that the amplitudes and the phases r_{xy} , r_z , θ , and α depend on Δ . For a better understanding of the complex spin structure, we plot a schematic view of this 16-site structure in Figs. 3(e) and (f). We found that this spin structure is consistent with the eigenvectors obtained from the classical analysis described in Sec.III.

Although the classical analysis totally ignores the quantum fluctuation effects, it still offers insight into the reason why the 16-site state has lower energy than the 120 degree state. In the region of $-1\text{meV} \lesssim \Delta \lesssim 20\text{meV}$, the lowest-energy mode (wavevector) in the classical

analysis is closer to the $q_y/(2\pi) = 1/4$ (the 16-site) than the $q_y/(2\pi) = 2/3$ (the 120 degree) (see Fig. 2(a,b)). Thus, the 16-site state is more favorable than the 120 degree state. This simple interpretation also explains why the 120 degree structure is stabilized for $\Delta \lesssim -1\text{meV}$: The lowest-energy mode of the classical analysis shows that the wavenumber approaches $q_y/(2\pi) = 2/3$ in this region.

Because the lowest modes are also close to $\mathbf{q}/(2\pi) = (1/\sqrt{3}, 1/5)$, one might speculate that a state characterized by this wavevector could be realized. However, that is not the case. Although we also calculated the energy using the iPEPS with 6×10 unit-cell, which is compatible with $\mathbf{q}/(2\pi) = (1/\sqrt{3}, 1/5)$, the energy was higher than that of the 16-site state. In this model, the state with $\mathbf{q}/(2\pi) = (1/\sqrt{3}, 1/5)$ does not appear as the ground state.

The 16-site state has eight-fold degeneracy: Z_4 from the lattice translation and Z_2 from the time reversal symmetries. In this case, we again expect a successive BKT transitions at nonzero temperatures with breaking of the Z_8 symmetry similar to the case of Z_6 symmetry³⁷.

4. Incommensurate phase

Finally, we investigate the incommensurate phase. In Fig. 7 (c), we show the energies obtained by iPEPS around the incommensurate phase. In the incommensurate phase, we obtained two types of large unit-cell structure depending on the unit-cell shape used in the iPEPS. In addition to the phase transition between the 16-site phase and these large unit-cell states around $\Delta \simeq 35$ meV, one can see the energy crossing between two distinct large unit-cell states around $\Delta \simeq 45$ meV indicated by an arrow. Although the second energy crossing may represent a phase transition, it could instead be “finite size effects” due to finite unit-cells used in the iPEPS. Actually, in the classical analysis, the characteristic wavevectors of the lowest-energy mode continu-

ously shift for $\Delta \gtrsim 35$ meV. It suggests the existence of the incommensurate phase in this region, the possibility of which in the quantum case is not excluded from the present analysis. Thus, we tentatively speculate that these two large unit-cell structures are a part of the incommensurate phase, where the Bragg wavenumber continuously moves with Δ in the thermodynamic limit.

V. CONCLUSIONS

In this paper, we have investigated the ground state properties of the realistic effective Hamiltonian for Na_2IrO_3 . Based on the three numerical methods, ED, DMRG and iPEPS, we have firmly established that the ground state of the *ab initio* Hamiltonian for Na_2IrO_3 is the zigzag(Z) state, in agreement with the experiment. In zigzag(Z) state, ferromagnetically-coupled chains are perpendicular to the z -bond and ordered spin moments are on the ac plane of Na_2IrO_3 . These features are also consistent with the experimental observation⁵⁻⁸.

On the other hand, the direction of the ordered moment predicted from our *ab initio* Hamiltonian, which is nearly parallel to $t(x, y, z) = (1, 1, 0)$ direction, does not match the analysis of experimental data implying the moment nearly parallel to the a axis (the $(1, 1, -2)$ direction)^{5,8}. In order to reproduce the precise direction, the weaker interactions ignored in the present *ab initio* Hamiltonian, such as the couplings between honeycomb layers, could be important. However, the experimental data are not from the single crystal and more definite determination of the direction is also desired.

We have also determined the ground state phase diagram of the Hamiltonian when the trigonal distortion Δ is monitored as a control parameter away from the *ab initio* value for Na_2IrO_3 . We have found, at least, five distinct magnetically ordered phases: the zigzag(X, Y), the zigzag(Z), the 120 degree structure, the 16-site structure, and the presumably incommensurate phase that appears as 48-site states in the present calculation. For large negative Δ region, zigzag(X, Y) states are stabilized. When we increase Δ , the direction of the ferromagnetically-coupled chain in the zigzag state rotates 120 degree forming zigzag(Z) state around $\Delta \simeq -44$ meV. In the middle of the phase diagram 120 degree structure appears in the narrow region. We have identified it as the 3-site and/or the 6-site order according to the result of the iPEPS calculations for infinite systems. When we increase Δ toward positive values, the 16-site phase is stabilized. Although the previous 24-site ED calculation has not identified this phase, we have found that it has a lower energy than that of the 120 degree structures in a wide region based on the DMRG and iPEPS calculations. For large positive Δ , we have found a presumable incommensurate state. Although it is difficult to prove the “true” incommensurate nature because of the limitation of finite-size systems (ED, DMRG) or the number of the independent tensors (iPEPS), the results indicate that its

magnetic unit cell is at least larger than that consisting of 48 spins. Since the trigonal distortion may be selectively controlled by substitution of elements in Na_2IrO_3 , the present results give a useful guideline to understand possible rich phase diagram based on the combined effort of the reliable *ab initio* approach and experimental progress.

The accuracy and reliability of the *ab initio* Hamiltonian has been established in the present study through the detailed comparison with the experimental indications: The present study by combining three independent and accurate numerical algorithms has enabled a reliable approach to the thermodynamic limit by keeping high accuracy of the result.

An interesting question untouched in the present study on the *ab initio* Hamiltonian and left for future studies is how we can approach the spin-liquid state starting from the magnetic Na_2IrO_3 under the normal pressure. Based on 24-site ED calculation, Yamaji *et al* pointed out that a lattice expansion from Na_2IrO_3 may stabilize a Kitaev-type spin-liquid state¹⁸. Since it was already shown that the iPEPS is able to describe the Kitaev spin liquid state reliably²¹, searching and designing the spin liquid state by using the combined DMRG or PEPS on the realistic and first-principles framework is an intriguing future subject.

ACKNOWLEDGMENTS

We thank S. Todo, T. Suzuki, and K. Harada for fruitful discussions. The computation in the present work is partly performed on computers at the Supercomputer Center, ISSP, University of Tokyo. The numerical package $\mathcal{H}\Phi$ ³⁸ is used for the exact diagonalization calculations. We thank the computational resources of the K computer provided by the RIKEN Advanced Institute for Computational Science through the HPCI System Research project (hp140136, hp140215, hp150211, hp160201) and the Computational Materials Science Initiative (CMSI) supported by Ministry of Education, Culture, Sports, Science, and Technology, Japan. The present work is financially supported by JSPS KAKENHI No. 25287097, No. 26287079, No. 15K17701, No. 15K17702 and No. 16H06345. This work was funded by ImPACT Program of Council for Science, Technology and Innovation (Cabinet Office, Government of Japan).

Appendix A: the *ab initio* Hamiltonian of Na_2IrO_3

In this appendix, we summarize the derivation of *ab initio* Hamiltonian of Na_2IrO_3 (1).

In order to derive the effective spin Hamiltonian from the *ab initio* Hamiltonian for t_{2g} electrons (8), we employ the second order perturbation theory: Here we take the Hamiltonian of an isolated iridium atom $\hat{H}_{\text{tri}} + \hat{H}_{\text{SOC}} + \hat{H}_U$ as an unperturbed Hamiltonian and the hopping

$J_{X,Y}$ (meV)	K'	J'	J''
	-23.9467619	2.0225331	3.2124194
	I'_1	I'_2	I''_2
	1.8470590	-8.4040133	-3.1148375
J_Z (meV)	K	J	
	-30.7439117	4.4421939	
	I_1	I_2	
	-0.3777579	1.0659292	
J_2 (meV)	$K^{(2nd)}$	$J^{(2nd)}$	
	-1.2250998	-0.8030967	
	$I_1^{(2nd)}$	$I_2^{(2nd)}$	
	0.9901792	-1.4245524	
J_3 (meV)	$K^{(3rd)}$	$J^{(3rd)}$	
	1.7161468	1.5996219	
	$I_1^{(3rd)}$	$I_2^{(3rd)}$	
	0.1203473	0.0476719	

TABLE II. Precise exchange interactions of the *ab initio* Kitaev-Heisenberg Hamiltonian at $\Delta = -28$ meV calculated from the second-order perturbation theory. In the third-neighbor interaction, we approximated it as the isotropic Heisenberg interaction by neglecting off-diagonal interactions I_1^{3rd} and I_2^{3rd} and by averaging diagonal interaction as $J_3 = (K^{(3rd)} + 2J^{(3rd)})/3$

$$|\Psi\rangle = \sum_{\{m_{r_1}, m_{r_2}, \dots, m_{r_i}, \dots\}} \text{Tr} \prod_{\mathbf{R}} (A_1[m_{1,\mathbf{R}}] | A_2[m_{2,\mathbf{R}}] \cdots A_i[m_{N,\mathbf{R}}] | m_{r_1} m_{r_2} \cdots m_{r_i} \cdots), \quad (\text{B1})$$

where $A_i[m]$ is a 4-rank tensor located at the vertex i of the honeycomb lattice with three virtual indices and one physical index, m , (see Fig. 8), and Tr means the contraction over virtual indices. In order to treat infinite system, we assume that the tensors are translationally invariant with a unit cell containing $N = L_x \times L_y$ sites, and $m_{\mathbf{r}} = m_{i,\mathbf{R}}$ means the i th spin on a unit cell located at \mathbf{R} (see Fig. 1). Note that this iPEPS ansatz with a unit cell is totally different from a finite $L_x \times L_y$ system with the periodic boundary condition. Although the same tensors repeatedly appear in the definition of the wave function, (namely, A_i does not depend on \mathbf{R} in Eq. (B1)), the spins on equivalent but different unit-cell sites can take different values $m_{i,\mathbf{R}}$. Thus, the iPEPS is able to take into account infinitely large spin degrees of freedom in contrast to the finite-size algorithm.

Our iPEPS calculations are conducted in two steps. The first step is optimization of the tensors and the second step is calculation of physical quantities.

In the first step, we optimize tensors using the imaginary-time evolution by multiplying $e^{\tau\mathcal{H}}$ repeatedly. The imaginary-time evolution operator is decomposed into a product of $e^{\tau\mathcal{H}_{ij}}$ with two-body interactions \mathcal{H}_{ij} using Suzuki-Trotter decomposition^{39,40}. Typically, we start from $\tau = 0.1/|K|$ and gradually decrease τ to $\tau = 0.001/|K|$ to reach the ground state accurately, where K is the largest exchange interaction of the model. In this

term \hat{H}_0 as a perturbation¹⁸. We consider the doubly generated ground state of $\hat{H}_{\text{tri}} + \hat{H}_{\text{SOC}} + \hat{H}_U$ for a single-site problem as a pseudospin. The exchange couplings among the pseudospins are derived through the second order perturbation theory by numerically diagonalizing the Hamiltonian $\hat{H}_{\text{tri}} + \hat{H}_{\text{SOC}} + \hat{H}_U$ ¹⁸.

In Table A, we show thus obtained exchange interactions which we used in our *ab initio* calculation of the ground state of Na_2IrO_3 . Note that for the third-neighbor interaction, we approximated it as the isotropic Heisenberg interaction where we neglected off-diagonal interactions ($I_1^{(3rd)}$ and $I_2^{(3rd)}$) and we averaged the diagonal interactions as $J_3 = (K^{(3rd)} + 2J^{(3rd)})/3$.

Appendix B: iPEPS calculation method

In this appendix, we describe methods used in iPEPS calculations. In our calculation, we first represent the ground-state wave-function $|\Psi\rangle$ of the model as a tensor product state:

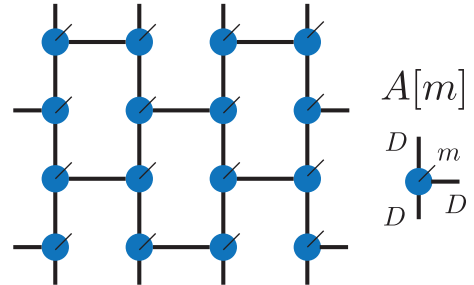


FIG. 8. (Color online) Schematic picture of iPEPS tensor network for Honeycomb lattice. Tensor A has a physical index and three virtual indices. The dimension of the physical index is $m = 2$ in the case of $S = 1/2$ spin system. The dimension of the virtual indices is set to D , which determines the accuracy of the iPEPS wave function for the ground state. The iPEPS becomes exact in the limit $D \rightarrow \infty$ and the accuracy is improved systematically with increasing D .

imaginary-time evolution, we need a truncation in order to keep the bond-dimensions of the tensor $A_i[m]$ within a tractable size. For this truncation we use so called the simple-update method²⁹. In this simple-update method we insert diagonal matrices $\lambda_{i,j}$ on the bond connecting virtual indices and they are considered as mean-field like environments at the truncation (see Fig. 9(a)). For

the nearest-neighbor interactions, we use the singular value decomposition (SVD) and truncate smaller singular values²⁹.

In the presence of further neighbor interactions, we need to treat at least three tensors simultaneously because the tensors A_i and A_j interacting through a further-neighbor interaction are not directly connected in our tensor network. In order to treat further-neighbor interaction, we connect A_i and A_j through other intermediate tensor(s) and consider the imaginary-time evolution of the cluster as shown in Fig. 9(a). In order to construct the clusters, we use the smallest cluster (the shortest path). If there are more than one smallest clusters, we decompose the imaginary-time evolution. For instance, if two smallest clusters exist, we decompose it as $e^{\tau\mathcal{H}_{ij}} = e^{\tau\mathcal{H}_{ij}/2}e^{\tau\mathcal{H}_{ij}/2}$, and assign the different cluster to each of $e^{\tau\mathcal{H}_{ij}/2}$. In the case of the *ab initio* Kitaev-Heisenberg Hamiltonian, the smallest cluster is unique for J_2 interaction (see Fig. 10(a)), while there are two types of the smallest cluster for J_3 interactions (see Figs. 10(b) and (c)).

In order to decompose the cluster, we use symmetric decomposition by constructing projectors, which is slightly different from the decomposition using successive SVDs⁴¹.

In the case of a cluster consisting of three tensors, first we construct a cluster by combining three A tensors, mean-field like environments $\sqrt{\lambda}$, and the imaginary-time evolution operator as shown in Fig. 9 (a). Note that we can see the cluster as a one-dimensional chain shown in the left part of Fig. 9(a), where for the sake of flowing calculations we introduce the matrix product operator (MPO) representation of the imaginary-time evolution operator.

Next, we perform two SVDs which decompose the cluster into 2 + 1 and 1 + 2 segments (see Fig. 9(b)). From these SVDs, we obtain two sets of tensors and singular values, $(U_r, \lambda_r, V_r^\dagger)$ and $(U_l, \lambda_l, V_l^\dagger)$.

Then, we construct two pairs of projectors (P_r, \tilde{P}_r) and (P_l, \tilde{P}_l) by using tensors obtained by the previous SVDs as shown in Fig. 9(c). Note that these projectors satisfy the relation $\tilde{P}P = \text{identity}$.

Finally, we insert projectors into the cluster (Fig. 9(d)) and decompose it into three parts to obtain updated tensors. The updated tensors are defined as Fig. 9 (e).

For larger clusters we can use the same method by considering several SVDs and creating projectors. In the actual calculation, we perform QR decomposition of tensors A_i and A_j before applying imaginary-time evolution operator in order to reduce the computational cost^{42,43}.

In the second step, we calculate expectation values from the obtained wave function. In this step, we use the approximate contraction based on the corner transfer matrix (CTM) method³⁰⁻³⁶. In order to treat the several unit-cell shapes, we use the directional CTM renormalization group³⁰, with the generalization to arbitrary unit-cell sizes^{35,36}. As the bond dimension χ of the CTMs, we typically use $\chi = D^2$ because further increase of χ be-

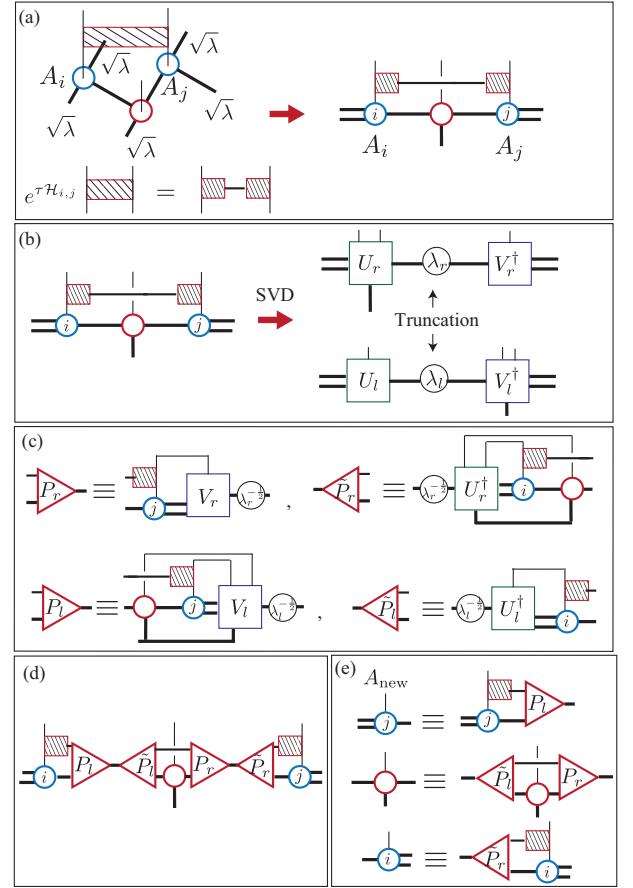


FIG. 9. (Color online) Procedure of imaginary-time evolution for the second neighbor interaction. Blue and red circles with legs represent tensor A defined in Eq. (B1), where thick lines are virtual bonds and a vertical thin line is the physical bond (see also Fig. 8). A shaded rectangle represents the imaginary-time evolution operator $e^{\tau\mathcal{H}_{i,j}}$. (a) A cluster consisting of three tensors (A_i , A_j (blue) and an intermediate tensor (red)) and an imaginary-time evolution operator with mean field like environment ($\sqrt{\lambda}$). Note that because we use tensors defined in Eq. (B1), each tensor includes $\sqrt{\lambda}$ implicitly. Thus, $\sqrt{\lambda}$ is sufficient as the mean-field like environment for the simple update. By using a matrix product operator representation of $e^{\tau\mathcal{H}_{i,j}}$, we can transform the cluster into a one-dimensional chain representation shown in the left side. (b) Two types of SVDs which decompose the cluster into 2 + 1 (top) or 1 + 2 (bottom) segments. Here we truncate the tensor by keeping only the largest D singular values. (c) Construction of two pairs of projectors (P_r, \tilde{P}_r) and (P_l, \tilde{P}_l) . $U_r^\dagger, U_l^\dagger, V_r$ and V_l are complex conjugates of the tensors obtained by SVDs in the step (b). (d) We approximate the original cluster by inserting the projectors calculated in the step (c). (e) Definition of updated tensors A_{new} .

yond D^2 did not change expectation values largely in the case of magnetically ordered phase we observed.

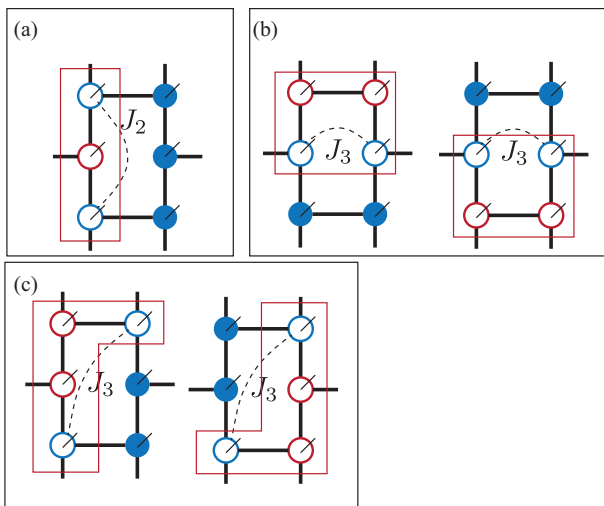


FIG. 10. (Color online) Schematic pictures representing the smallest clusters used in imaginary-time evolutions for further neighbor interactions. Blue open circles represent tensors interacting through a further-neighbor interaction. Red open circles are intermediate tensors. The smallest clusters are indicated by red rectangles. (a) In the case of the second-neighbor interaction, the smallest cluster is uniquely determined. (b,c) In the case of the third-neighbor interactions, there are two types of the smallest cluster.

Appendix C: iPEPS calculation for the nearest neighbor model

In this appendix, to compare with the full *ab initio* studies and to gain further insights, we briefly show the analysis on a simplified nearest-neighbor *ab initio* Hamiltonian for Na_2IrO_3 where we neglect the second and the third neighbor interactions and consider only the nearest-neighbor interactions. For this analysis, we use tensor network methods with the iPEPS ansatz. In the case of the nearest-neighbor interaction, we can easily apply the so called “full update” method^{26,30}, which is expected to be more accurate than the simple update used in the analysis of the main part. By considering the nearest-neighbor interaction only, we can compare the results obtained by the simple update and the full update, and estimate the reliability of simple update method.

In Fig. 11(a), we show the energy of the nearest-neighbor *ab initio* Hamiltonian as a function of the bond dimension D . Although the energies obtained by the full update method is slightly lower than those of the simple update at the same D , the difference is quite small

compared with the decrease in the energy with increasing the bond dimension. Thus, the simple update seems to be sufficiently reliable for the present *ab initio* Hamiltonian whose ground state is expected to be a magnetically ordered state.

In order to further investigate the nature of the ground state, we show the spin correlation along the y -direction (see Fig. 1) in Fig. 11(b). One can see that the spin corre-

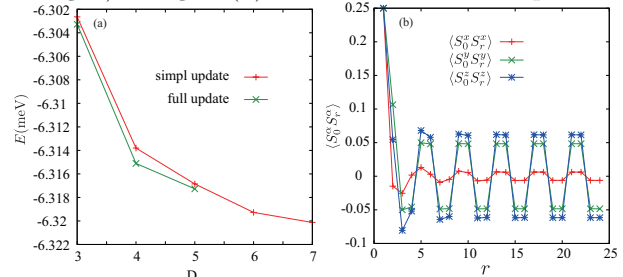


FIG. 11. (Color online) (a) Bond-dimension (D) dependence of the energy of the nearest-neighbor *ab initio* Hamiltonian calculated by the iPEPS optimized by using the simple update and the full update with the $L_x \times L_y = 2 \times 4$ unit cell. (b) Spin-spin correlation function of S^x , S^y , and S^z along the y -direction obtained by iPEPS with the simple update ($D = 7$).

lation shows four-site periodicity, which is totally different from the zigzag(Z) structure observed in the ground state of *ab initio* Hamiltonian including the second and the further neighbor interactions. Indeed, the ground state of the nearest-neighbor *ab initio* Hamiltonian is an 8-site state different from the zigzag(Z) state. Thus, in order to obtain the experimentally observed zigzag(Z) state, the further-neighbor interactions are crucially important.

Note that the iPEPS has been able to describe the Kitaev spin liquid state by using the full update optimization if it is applied to the Kitaev-Heisenberg model²¹. Therefore, the method is capable of describing the Kitaev spin liquid in general. Nevertheless, we did not obtain the spin liquid state for a more realistic Hamiltonian with only the nearest-neighbor interaction truncated from the *ab initio* Hamiltonian even if we used the full update. Furthermore, the further-neighbor interactions stabilize the magnetically ordered state rather than the Kitaev spin liquid, as we see in the ground state of the full *ab initio* Hamiltonian, which includes the second and the third neighbor interactions. Therefore, our result shows that the magnetic order rather than the spin liquid is robust around the *ab initio* parameter values, consistently with the experimental results.

* t-okubo@issp.u-tokyo.ac.jp

¹ G. Jackeli and G. Khaliullin, Phys. Rev. Lett. **102**, 017205 (2009).

² J. c. v. Chaloupka, G. Jackeli, and G. Khaliullin,

Phys. Rev. Lett. **105**, 027204 (2010).

³ X. Wan, A. M. Turner, A. Vishwanath, and S. Y. Savrasov, Phys. Rev. B **83**, 205101 (2011).

⁴ W. Witczak-Krempa, G. Chen, Y. B. Kim, and L. Balents,

- Annual Review of Condensed Matter Physics **5**, 57 (2014).
- ⁵ X. Liu, T. Berlijn, W.-G. Yin, W. Ku, A. Tsvelik, Y.-J. Kim, H. Gretarsson, Y. Singh, P. Gegenwart, and J. P. Hill, Phys. Rev. B **83**, 220403 (2011).
 - ⁶ S. K. Choi, R. Coldea, A. N. Kolmogorov, T. Lancaster, I. I. Mazin, S. J. Blundell, P. G. Radaelli, Y. Singh, P. Gegenwart, K. R. Choi, S.-W. Cheong, P. J. Baker, C. Stock, and J. Taylor, Phys. Rev. Lett. **108**, 127204 (2012).
 - ⁷ F. Ye, S. Chi, H. Cao, B. C. Chakoumakos, J. A. Fernandez-Baca, R. Custelcean, T. F. Qi, O. B. Korneta, and G. Cao, Phys. Rev. B **85**, 180403 (2012).
 - ⁸ S. W. Lovesey and A. N. Dobrynin, Journal of Physics: Condensed Matter **24**, 382201 (2012).
 - ⁹ Z. Alpichshev, F. Mahmood, G. Cao, and N. Gedik, Phys. Rev. Lett. **114**, 017203 (2015).
 - ¹⁰ Y. Singh, S. Manni, J. Reuther, T. Berlijn, R. Thomale, W. Ku, S. Trebst, and P. Gegenwart, Phys. Rev. Lett. **108**, 127203 (2012).
 - ¹¹ A. Kitaev, Annals of Physics **321**, 2 (2006), january Special Issue.
 - ¹² I. Kimchi and Y.-Z. You, Phys. Rev. B **84**, 180407 (2011).
 - ¹³ J. c. v. Chaloupka, G. Jackeli, and G. Khaliullin, Phys. Rev. Lett. **110**, 097204 (2013).
 - ¹⁴ Y. Sizyuk, C. Price, P. Wölfle, and N. B. Perkins, Phys. Rev. B **90**, 155126 (2014).
 - ¹⁵ S. Bhattacharjee, S.-S. Lee, and Y. B. Kim, New Journal of Physics **14**, 073015 (2012).
 - ¹⁶ J. G. Rau, E. K.-H. Lee, and H.-Y. Kee, Phys. Rev. Lett. **112**, 077204 (2014).
 - ¹⁷ V. M. Katukuri, S. Nishimoto, V. Yushankhai, A. Stoyanova, H. Kandpal, S. Choi, R. Coldea, I. Rousochatzakis, L. Hozoi, and J. van den Brink, New Journal of Physics **16**, 013056 (2014).
 - ¹⁸ Y. Yamaji, Y. Nomura, M. Kurita, R. Arita, and M. Imada, Phys. Rev. Lett. **113**, 107201 (2014).
 - ¹⁹ J. G. Rau and H.-Y. Kee, arXiv:1408.4811 (2014).
 - ²⁰ Y. Yamaji, T. Suzuki, T. Yamada, S.-i. Suga, N. Kawashima, and M. Imada, Phys. Rev. B **93**, 174425 (2016).
 - ²¹ J. Osorio Iregui, P. Corboz, and M. Troyer, Phys. Rev. B **90**, 195102 (2014).
 - ²² Villain, J., Bidaux, R., Carton, J.-P., and Conte, R., J. Phys. France **41**, 1263 (1980).
 - ²³ K. Shinjo, S. Sota, and T. Tohyama, Phys. Rev. B **91**, 054401 (2015).
 - ²⁴ F. Verstraete and J. I. Cirac, Phys. Rev. A **70**, 060302 (2004).
 - ²⁵ F. Verstraete and J. I. Cirac, arXiv:cond-mat/0407066 (2004).
 - ²⁶ J. Jordan, R. Orús, G. Vidal, F. Verstraete, and J. I. Cirac, Phys. Rev. Lett. **101**, 250602 (2008).
 - ²⁷ M. A. Martín-Delgado, M. Roncaglia, and G. Sierra, Phys. Rev. B **64**, 075117 (2001).
 - ²⁸ T. Nishino, Y. Hieida, K. Okunishi, N. Maeshima, Y. Akutsu, and A. Gendiar, Progress of Theoretical Physics **105**, 409 (2001).
 - ²⁹ H. C. Jiang, Z. Y. Weng, and T. Xiang, Phys. Rev. Lett. **101**, 090603 (2008).
 - ³⁰ R. Orús and G. Vidal, Phys. Rev. B **80**, 094403 (2009).
 - ³¹ R. J. Baxter, Journal of Mathematical Physics **9** (1968).
 - ³² R. J. Baxter, Journal of Statistical Physics **19**, 461 (1978).
 - ³³ R. J. Baxter, *Exactly Solved Models in Statistical Mechanics* (Academic Press, London, 1982).
 - ³⁴ T. Nishino and K. Okunishi, Journal of the Physical Society of Japan **67**, 3066 (1998).
 - ³⁵ P. Corboz, S. R. White, G. Vidal, and M. Troyer, Phys. Rev. B **84**, 041108 (2011).
 - ³⁶ P. Corboz, T. M. Rice, and M. Troyer, Phys. Rev. Lett. **113**, 046402 (2014).
 - ³⁷ J. V. José, L. P. Kadanoff, S. Kirkpatrick, and D. R. Nelson, Phys. Rev. B **16**, 1217 (1977).
 - ³⁸ $\mathcal{H}\Phi$ is available at <https://github.com/QLMS/HPhi>.
 - ³⁹ M. Suzuki, Progress of Theoretical Physics **56**, 1454 (1976).
 - ⁴⁰ H. F. Trotter, Proceedings of the American Mathematical Society **10**, 647 (1950).
 - ⁴¹ P. Corboz, J. Jordan, and G. Vidal, Phys. Rev. B **82**, 245119 (2010).
 - ⁴² L. Wang, I. Pižorn, and F. Verstraete, Phys. Rev. B **83**, 134421 (2011).
 - ⁴³ S. Depenbrock and F. Pollmann, Phys. Rev. B **88**, 035138 (2013).